I&EC research
Industrial & Engineering Chemistry Research

pubs.acs.org/IECR

Article

Semiempirical Model of the Drag Force Acting on an Obstacle in Downward Dense Particle Flows as per the Flow-Around Behavior

Xiandong Liu, Hairui Yang, Hai Zhang, Junfu Lyu, and Yang Zhang*

Cite This: *Ind. Eng. Chem. Res.* 2023, 62, 3001−3010

Read Online

ACCESS | Metrics & More | Article Recommendations | Supporting Information

ABSTRACT: Determination of the flow-around drag force acting on an internal when particles downwardly flow around the internal is important for the safety of internals in the downward particle flow channel. In this study, the flow behaviors of particles downwardly flowing around different obstacles were investigated and a semiempirical drag force model was proposed based on the characteristics of the flow patterns. The proposed model was validated and key coefficients were correlated using the experimental data. The results indicate that there were three featured flow zones when particles downwardly flowed around an obstacle: the flow stagnant zone (disappear for triangular/conical obstacle), the slip-shear flow zone, and the flow separation zone. The stagnant zone angle and the flow separation angle were proposed to depict transition points of three flow zones when particles flowed around a cylindrical/spherical obstacle, and the two angles were found independent of the flow condition. A drag force model as per the flow patterns was proposed. The model decomposed the drag force into the compression force, the shear force, and the confinement force. The expressions of the compression stress, the shear stress, the effective area, and the confinement force were given. The mathematical form of the proposed model was validated and key coefficients in this model were also correlated using the experimental data. The average error of the drag force model was ±7.6% while the maximum error was within ±15%.

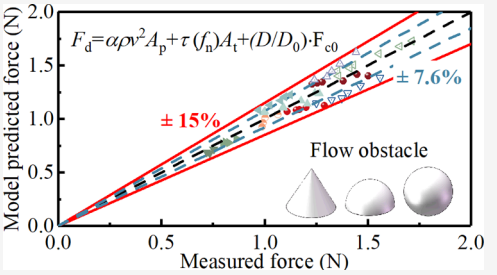

1. INTRODUCTION

Dense downward particle flow is a common particle flow state and is widely applied in various particle transport equipment or chemical reactors (circulating fluidized bed,[1] silos,[2] moving bed heat exchanger,[3] chemical looping combustion reactor,[4] etc.). In a downward particle flow channel, it is common to arrange internals to adjust the flow state[5] or to serve as heat exchange tubes.[6] Also, the installed intrusive measurement equipment[7] can be viewed as another kind of internal. The drag forces acting on the arranged internals when particles flow around it may result in vibration, material fatigue, or even failure of the whole internal.[8] Therefore, it is worth investigating the force acting on internals in downward particle flow channels for optimizing the strength and structure design of immersed internals.

Many researchers have studied the flow-around drag force acting on an obstacle when dense particles flow around it, and it was found that the drag force and its prediction model are different under different flow-around processes. R. Albert[9] investigated the drag force acting on a vertical cylinder rod in a rotating bucket filled with grains and obtained an empirical force model corresponding with particle density, insert depth, and diameter of the rod. Liu et al.[10] studied the drag force acting on a horizontal cylinder rod when it moved in a granular bed. The drag force was not correlated with apparent parameters but was calculated by the integral of particle stress based on the flow-around flow field and quoted theoretical stress model. Brzinski III et al.[11] arranged a rotating horizontal rod in a fluidized bed and measured the drag force. The results indicated that the model of drag force in a fluidized bed has to add a parameter depicting the degree of fluidization (the ratio of superficial gas velocity to minimum fluidization velocity was adopted for their work) and thus a different drag force model was proposed. Besides the flow-around process of a rod moving in a packed/fluidized bed, granular matter downwardly flowing around a cylinder,[12] particles flowing around a sphere in a horizontal tube,[13] and a sphere dropping down into a packed/fluidized bed[14,15] were studied and different models were proposed. There were also studies trying to establish a uniform drag force model applied for all kinds of flow-around processes, but the prediction accuracy decreased dramatically. Faug[16] reviewed a great number of drag force data and found that there is a maximum error of two orders of magnitude if a unified drag force model was applied to them. Considering that the unified model remains an unsolved problem, and the drag force model for the form of particles downwardly flowing around an obstacle is still lacking, it is necessary to investigate

Received: November 7, 2022
Revised: January 18, 2023
Accepted: January 19, 2023
Published: January 30, 2023

https://doi.org/10.1021/acs.iecr.2c04034
Ind. Eng. Chem. Res. 2023, 62, 3001−3010

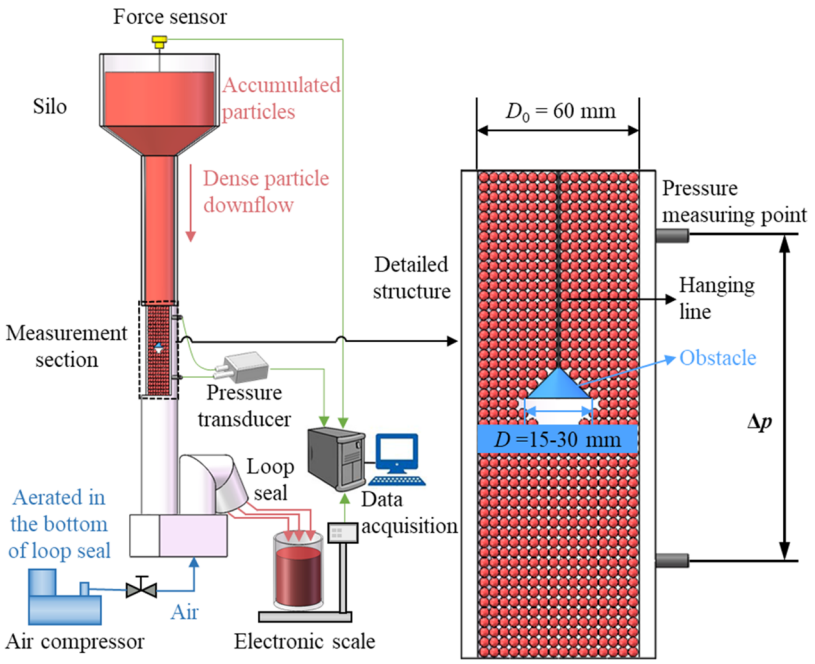

Figure 1. Schematic diagram of the system of the drag force measurement.

this drag force acting on internal obstacles in dense particle flows and develop its prediction model.

To develop a drag force model, the method of first observing/simulating flow-around behaviors and then detecting flow characteristics to derive models was adopted by many studies. Jiang et al.[17] experimentally studied the flow characteristics of the process of granular flows impacting a wall-like obstacle and quantitatively determined the size of the flow dead zone. Through the force analysis on the dead zone and wall-like obstacle, the expression of the impact force was derived and a semiempirical model was further proposed with some parameter fittings. Clark[18] applied photoelastic tomography technology to investigate the flow field of the process of a sphere falling into a packed bed and to obtain the local granular response on the front end of the falling sphere. With the knowledge of quantitative flow information, a multiplicative stochastic term was supplemented into the former empirical drag force model. Roth et al.[19] simulated the process of a cylindrical rod vertically intruding a packed bed and found the particle flow behavior transitioned from inertial to quasi-static behavior. With a better understanding of this physical process, the microscopic interpretation and calculation method of the empirical term in the original model could be provided. In the aforementioned studies, the drag force models were developed based on the observation of the flow-around behaviors, providing clear physical essence.

In this work, to obtain an insightful understanding of the particle flow behaviors, stained particle image velocimetry (SPIV) technology proposed by our previous work[20] was applied to particle flows downwardly flowing around an obstacle. An equation calculating the drag force was derived as per the measured flow characteristics and was correlated using the experimental data of the drag force acting on different internal obstacles at different particle flow velocities. After the correlation and parameter fitting, a semiempirical model of the downwardly flowing-around drag force of particle flows suitable for a wide range of particle velocities and obstacles was proposed.

2. EXPERIMENTAL APPROACH

2.1. Experimental Equipment for Drag Force Measurements. Experiments were conducted to study the behaviors of dense particle flow passing around an obstacle. The flow characteristics were investigated in a quasi-two-dimensional experimental system using the SPIV technology proposed in our previous work. Detailed information about this technology and the experiment system can be found in ref 20 To further investigate the drag force, another three-dimensional experimental system was established and is schematically shown in Figure 1. The measurement section of the rig was a vertical cylindrical flow channel with an inner diameter D_0 of 60 mm. A silo was connected to the top of this measurement section to feed the particles. A loop seal as a pneumatic valve was connected at the bottom of the measurement section. The fluidization air, provided by an air compressor, was distributed using the loop seal to fluidize the particles and control the outflow apparent mass flux, $\dot{m}$. The outlet particles were collected by a bucket placed on an electronic scale. The real-time accumulated particle mass was recorded by the electronic scale, and thereby the real-time particle mass flux was obtained by deriving the accumulated particle mass with respect to time. With the knowledge of the bulk density of flow material, the apparent flow velocity was further calculated by the quotient of mass flux and bulk density. In the experiments, the humidity was not especially controlled, but the laboratory was kept dry and the relative humidity of the laboratory was kept at 10−20%.

The drag force was measured by the hanging method. The targeting obstacle was hung in the center of the cross section by a hanging line connected to a force sensor arranged above the silo. The force sensor recorded the drag force acting on the obstacle (the vertical component of all of the force, and the horizontal component was neglected since it was offset) in real-time and the sampling frequency was 10 Hz. To eliminate the influence of the hanging line, the line was a steel wire rope with a diameter of 0.6 mm, and a blank test was done first to

https://doi.org/10.1021/acs.iecr.2c04034
Ind. Eng. Chem. Res. 2023, 62, 3001−3010

eliminate the error caused by the drag force on the hanging line. For each working condition, the measurement time was at least 10 s and the average force of the steady section was considered as the drag force under this flow velocity. Meanwhile, two pressure measuring points were arranged at 50 mm above and below the targeting obstacle, respectively, and the pressure drop between the two measuring points was measured by a pressure transducer.

The flow material was a mixture of transparent glass beads and red-stained glass beads, and the latter served as the tracer for the measurement of flow behavior. The real density of the glass beads ρ_p was 2504 kg/m^3, and the bulk density of the mixture ρ_b was 1454 kg/m^3. The particle size distribution is shown in Figure 2, and the average diameter of the particles (d_{50}) was 143.2 μm.

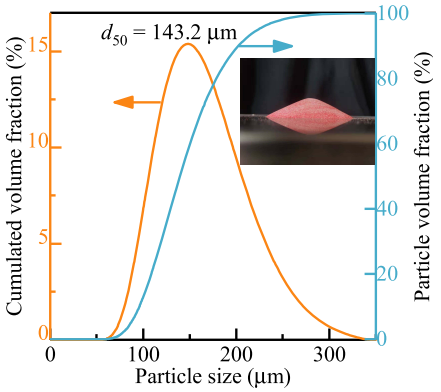

Figure 2. Size distribution of the flow material.

2.2. Data Processing Method. The method of evaluating the measured data (including the flow velocity, drag force, and pressure drop) was introduced in this section. Concerning the flow velocity, since outflow particles were collected and the curve of collected mass versus time (shown in Figure 3a) showed a linear relationship, the flow velocity in a certain working condition was viewed as stable and was calculated by the ratio of apparent mass flux of bulk density, expressed as eq 1

$$v = \frac{\dot{m}}{\rho_b} \tag{1}$$

Concerning the drag force and the pressure drop, the measured data of a typical working condition (particles flowing around a sphere with the diameter of 20 mm under an apparent flow velocity of 0.17 m/s, as shown in Figure 3b) was taken as an example to shown their evaluation methods. In this working condition, the force signal took about 3 s to reach the steady state and then decreased gradually at the end of one test. The decrease in the measured force was attributed to the change in the fluidization state. As particles flow out, the material height level kept decreasing and the sealing effect decreased. The fluidization state changed a lot as the particles above the measurement section became less. Therefore, the average values of the steady section on the curves of force F_1 and pressure drop Δp were selected as the measured steady-state F_1 and Δp results processed in this study (shown in Figure 3b). The curve of the measured force in the blank test was also shown in Figure 3b and a similar data processing method was applied to obtain its mean value F_0. The drag force F_d for this working condition was thereby calculated using eq 2

$$F_d = F_1 - F_0 \tag{2}$$

2.3. Experimental Equipment for Shear Stress Measurements. Particle shear stress is a key parameter in the drag force model (a detailed explanation is given in Section 3.2) and a measurement system for the particle shear stress was established. This test rig (schematically shown in Figure 4a) was a typical Couette rheometer widely applied in the measurement of particle shear stress,[21,22] and particles used in the shear stress measurements were the same as those in Section 2.1 to ensure the consistency of results. This Couette rheometer consisted of a fixed outer cylinder with the inner diameter of 140 mm, an inner rotating cylinder with the outer diameter of 110 mm, and an air distributor at the bottom. The outer cylinder was made of quartz glass to reduce the electrostatic effect between particles and walls. The inner cylinder was made of steel. The inner cylinder was connected to an electric motor through a shaft mounted on its axis and was controlled to rotate at selected speeds. The shaft was also installed with a precalibrated torque sensor (range: 0−1 N·m;

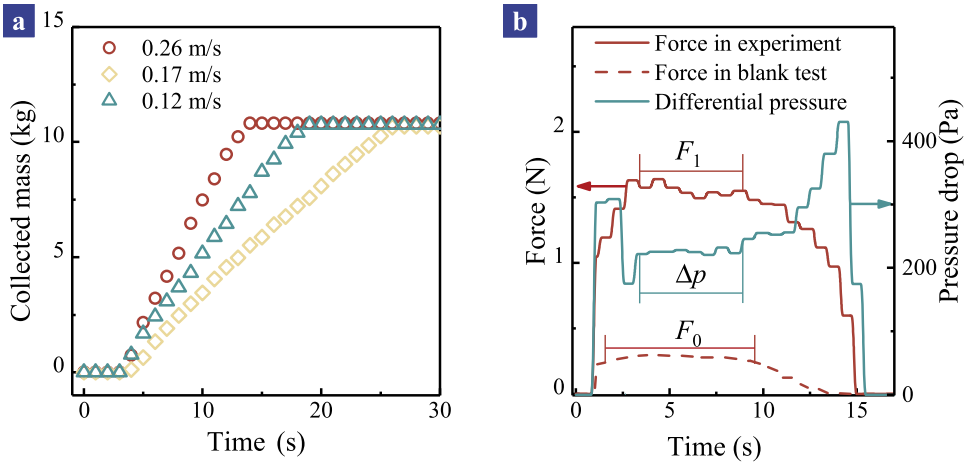

Figure 3. Data acquisition of the experimental system. (a) Real-time collected particle mass versus time under conditions of particles flowing around a sphere with the diameter of 20 mm at three different flow velocities (0.12, 0.17, 0.26 m/s). (b) Measured signals of force and pressure drop in a typical working condition: particles flowing around a sphere with the diameter of 20 mm under an apparent flow velocity of 0.17 m/s.

https://doi.org/10.1021/acs.iecr.2c04034
Ind. Eng. Chem. Res. 2023, 62, 3001−3010

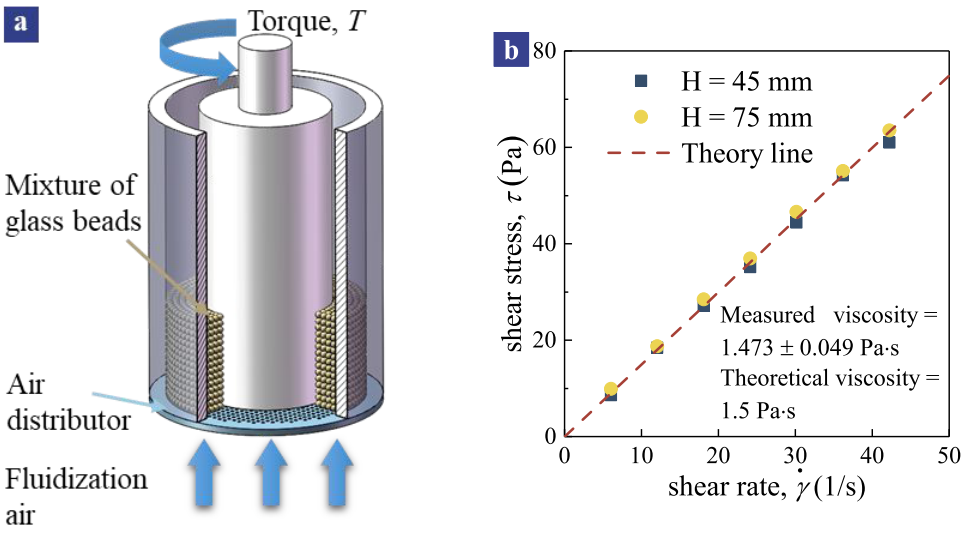

Figure 4. Measurement system for particle shear stress. (a) Schematic diagram of the experimental system of the particle shear stress measurement. (b) Validation of the measurement system: dashed line: theoretical values of glycerol 99% (μ = 1.5 Pa·s); teal box solid: experiment points, the height of liquid level H = 45 mm; and yellow circle solid: experiment points, the height of liquid level H = 75 mm.

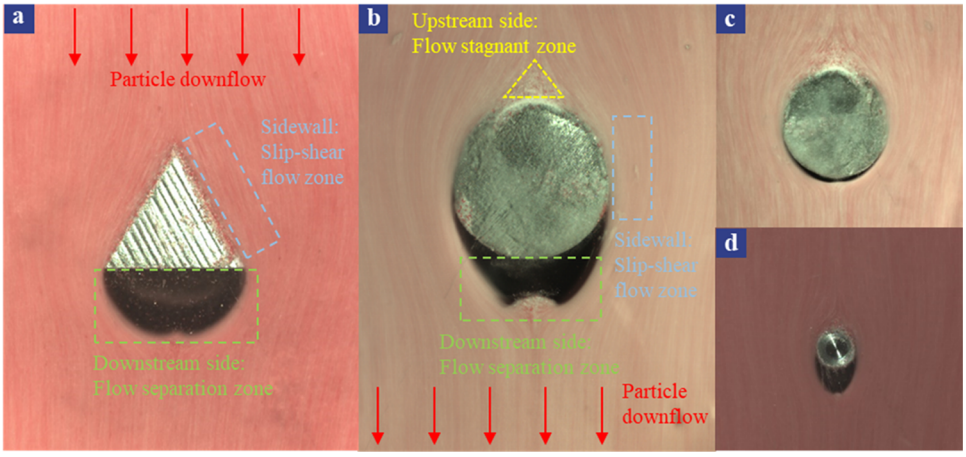

Figure 5. Flow characteristics of dense particle flow-around process shown by long exposure pictures (t_e = 0.1 s). (a) Slip-shear flow zone and flow separation zone. The side length of the equilateral triangular column: 17 mm, v = 0.08 m/s. (b) Flow stagnant zone, slip-shear flow zone, and flow separation zone. Diameter of the cylindrical obstacle: 20 mm, v = 0.15 m/s. (c) Diameter of the cylindrical obstacle: 20 mm, v = 0.05 m/s. (d) Diameter of the cylindrical obstacle: 5 mm, v = 0.10 m/s.

measurement error: 0.1% of the full scale) to measure the applied torque. To avoid particles slipping at the wall of the rotating inner cylinder, the inner cylinder was lined with a thin layer of adhesive tape with particles (same as flow material) glued to the side in contact with the flowing particles. In the experiment, particles were initially packed in the apparatus and the fluidization air was then supplied in the bottom to fluidize it at different fluidization states. The air was provided by an air compressor and the air flux was controlled by a mass flow controller. An air distributor (a perforated plate with an opening ratio of 1.1%) was arranged at the bottom of the apparatus to evenly distribute the fluidization air. During the experiment, after the fluidization state became steady, the electric motor drove the inner cylinder to rotate at a specific speed, and the torque T produced by particle shear was measured by the torque sensor. The shear rate $\dot{\gamma}$ at a certain rotation speed ω (rpm) was calculated by eq 3

$$\dot{\gamma} = \frac{\frac{\omega}{60} 2\pi R_1}{R_2 - R_1} \tag{3}$$

where R_1 and R_2 are the outer and inner radii of the inner and outer cylinders, respectively. The particle shear stress τ on the inner cylinder was calculated by eq 4

$$\tau = \frac{T}{2\pi R_1^2 H} \tag{4}$$

where H is the particle packing height. In each test, the measuring time was kept for at least 60 s, and the average value of torque was adopted as the measured data. Before the particle shear test, the experiment system was tested with a Newtonian liquid with known viscosity (glycerol, 99% purity, and viscosity 1.5 Pa·s) to verify the validity of the experimental system. In this validation experiment, the air distributor at the bottom was substituted by a plate of the same size to prevent the glycerol from flowing out. The validation experiment was done with two different heights of liquid level and the results

https://doi.org/10.1021/acs.iecr.2c04034
Ind. Eng. Chem. Res. 2023, 62, 3001−3010

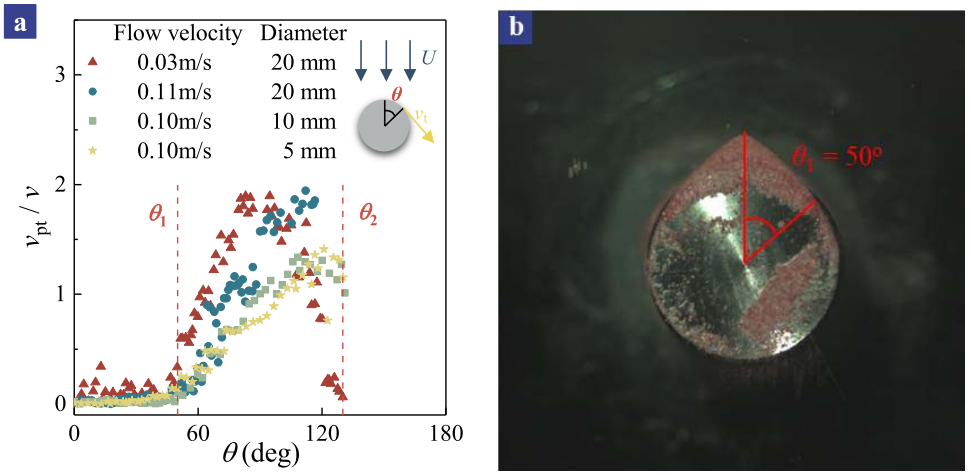

Figure 6. Determination of stagnant zone angle and flow separation angle. (a) Variation curve of particle tangential velocity to apparent velocity on the cylinder surface. Maroon box solid: obstacle: 20 mm cylinder, v = 0.03 m/s; teal circle solid: obstacle: 20 mm cylinder, v = 0.11 m/s; green triangle up solid: obstacle: 10 mm cylinder, v = 0.10 m/s; and yellow diamond solid: obstacle: 5 mm cylinder, v = 0.10 m/s. (b) Picture of the static packing of the flow material.

(shown in Figure 4b) indicated a good agreement with the theoretical values which proved the data validity.

3. RESULTS AND DISCUSSION

3.1. Flow Characteristics and Flow Fields. Using the SPIV technology proposed by our previous work,[20] the flow behaviors of particles downwardly flowing around different obstacles were investigated in this section. Figure 5 shows the flow characteristics of particles flowing around an equilateral triangular column or a cylindrical obstacle at different flow velocities. Videos of the particle motion can be also found in the Supporting Material. For a triangular obstacle (shown in Figure 5a), there are two obvious flow zones. Along the sidewall, particles slide along it, forming the slip-shear flow zone. The flow separation occurs below the bottom of the triangular obstacle, forming the flow separation zone on the downstream side. This phenomenon is analogous to that in the continuous fluid flowing around the triangular column (e.g., ref 23). The process of particles flowing around the cylindrical obstacle (shown in Figure 5b) is similar, but a flow stagnant zone forms on the upstream side of the cylindrical obstacle. This flow stagnant zone is also found in other similar particle flows (e.g., ref 24). Although the obstacle, size, and flow velocities are quite different in the present study, the key features of the particle flow behavior are similar and these distinctive zones are also exhibited in Figure 5c,d.

Quantitative depiction of the flow characteristics of the particles flowing around a triangular obstacle is relatively easy because the slip-shear flow zone only exists on the side surfaces and the flow separation zone only exists on the bottom surface. The transition points of the two flow zones are the two vertices at the bottom line of the triangle. However, to quantitatively describe the flow characteristics of cylindrical obstacles, it is needed to determine the transition points of three flow zones. The center angle of the end point of the flow stagnant zone is defined as the stagnant zone angle, θ_1, and that of the start point of the flow separation zone is defined as the flow separation angle, θ_2. These two angles can quantitatively depict the position of three flow zones and are defined using the distribution curve of the ratio of the particle tangential velocity v_{pt} on the cylinder surface to apparent bulk velocity v (shown in Figure 6a). In Figure 6a, the particle velocity was measured by the proposed SPIV technology. When the center angle θ is small which corresponds with the flow stagnant zone, the dimensionless velocity v_{pt}/v keeps zero. The end of the stagnant zone can thus be defined as the turning point of the velocity curve and the value of θ_1 keeps approximately the same as 50° for different cylinder diameters and different flow velocities. The measured value of the stagnant zone angle is also equal to that in the static packing test (shown in Figure 6b), which indicates that the stagnant zone angle is a parameter related to particle properties rather than a flow parameter. This finding is the same as those in other studies (e.g., ref 25) on particles flowing around cylinder obstacles. On the velocity curve shown in Figure 6a, the measured points disappear at a certain center angle, which is defined as the flow separation angle. It was found that the flow separation angle θ_2 can be viewed as independent of flow conditions and cylinder diameters and keeps the same at ~130°. This finding that the flow separation angle is just related to particle property is also adopted in other granular research.[26]

3.2. Theoretical Model for the Drag Force. With the knowledge of flow patterns and some quantitative flow parameters of particles flowing around an obstacle, the theoretical model for the drag force is then proposed. Particles flowing around conical and spherical obstacles were investigated and the force analysis based on flow patterns was conducted (shown in Figure 7). It is worth noticing that even though flow behaviors discussed in Section 3.1 were obtained in a quasi-2D experiment system, the particle flow in a 3D flow channel can be viewed to have same flow behaviors as that in a 2D flow channel.[27] Therefore, the key flow behavior parameters, e.g., stagnant zone angle and flow separation angle, of particles flowing around conical obstacles and spherical obstacles in this 3D setup are viewed as the same as those of the triangular column and the cylindrical obstacle discussed in Section 2.

Through the force analysis, the drag forces on these obstacles can be decomposed into the compression force F_p, shear force F_s from particles (rolling friction force was considered as part of the shear force), and confinement force F_c from the lateral wall of the flow channel. It was proposed by

https://doi.org/10.1021/acs.iecr.2c04034
Ind. Eng. Chem. Res. 2023, 62, 3001−3010

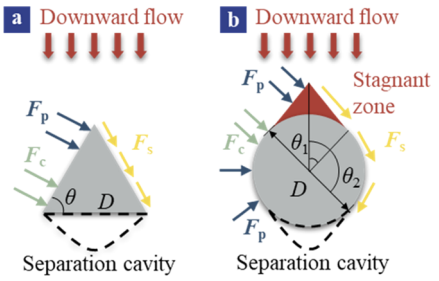

Figure 7. Flow patterns of particles flowing around conical and spherical obstacles and the decomposition of the drag force. (a) Vertical section of the process of particles flowing around a conical obstacle and (b) vertical section of the process of particles flowing around a spherical obstacle.

the literature[28] that when the ratio of the characteristic size of obstacle D to the size of the flow channel D_0, D/D_0, is larger than 0.2, the confinement of the walls on the obstacle cannot be neglected. The experiments in the literature[28] were carried out using similar particles to our research, so this conclusion was adopted in this work and the confinement force from the lateral wall was taken into consideration. These three components were analyzed respectively and their models were proposed.

The drag force F_p and F_s from particles can be expressed as the integrals of the compression stress p and shear stress τ on the effective area of the obstacle, respectively. It is worth noting that the area corresponding with the cavity at the bottom of the obstacle caused by the flow separation is not considered as the effective contact surface because there is no particle contact and only gas phase force exists. The drag force of the pure gas phase flowing around an obstacle (obtained through the theoretical calculation[29]) is approximately five orders of magnitude lower than that of particles flowing around the same obstacle (obtained through the measurement of the drag force in the following sections), so it is reasonable to neglect the force on the separation cavity. For a conical obstacle, the effective contact area is the side surfaces. For a spherical obstacle, the flow stagnant zone can be viewed as part of the obstacle, so the effective contact area is the side surfaces of the stagnant zone and part of the side surface of the sphere (surface corresponding with the center angle of $\theta_1-\theta_2$). Through the theoretical analysis above, the drag force from particles can be expressed by eq 5

$$F_p + F_s = \int_{S_e} (p \cos\theta + \tau \sin\theta) dS \tag{5}$$

where S_e is the effective stressed area, p the compression stress, τ the shear stress, and θ the base angle for conical obstacles and the center angle for spherical obstacles. Concerning the compression stress p, it is viewed as proportional to ρv^2 in granular,[30] fluidized bed[11] or fluid flow.[31] Our model followed this assumption and the compression stress is expressed by eq 6

$$p = \alpha \rho v^2 \tag{6}$$

where α is an empirical coefficient and is assumed to be the same on the whole effective contact surface. Concerning the shear stress τ, it was directly measured by the shear stress experiment system mentioned in Section 2.3. With this apparatus, particles were controlled under different fluidization states and the particle shear stresses were measured with the particle packing height of 52 mm. The range of shear rates in this experiment was 11.3−39.6 1/s, and it covered the range of particle shear rates measured in Section 3.1 (17.2−39.0 1/s), which proved the applicability of this experiment. The results (shown in Figure 8a) indicated that the particle shear stress does not change with the change of the shear rate but changes with the change of the fluidization state. This phenomenon was similar to the findings in the literature (*e.g.*, ref 32, 33). Meanwhile, the measured values of particle shear stresses (200−600 Pa) were similar to those measured in the literature[33] (100−300 Pa, the difference in measured values was due to the difference in particles), which proved our measurement results. The parameter of fluidization number f_n is defined to quantitatively represent the fluidization state. The fluidization number f_n is expressed by the ratio of gas−solid slip velocity u_{slip} to the minimum fluidization velocity u_{mf}, as shown by eq 7

$$f_n = \frac{u_{slip}}{u_{mf}} \tag{7}$$

When the fluidization number is equal to 0, it represents the state of the packed bed; when it is equal to 1, it represents the

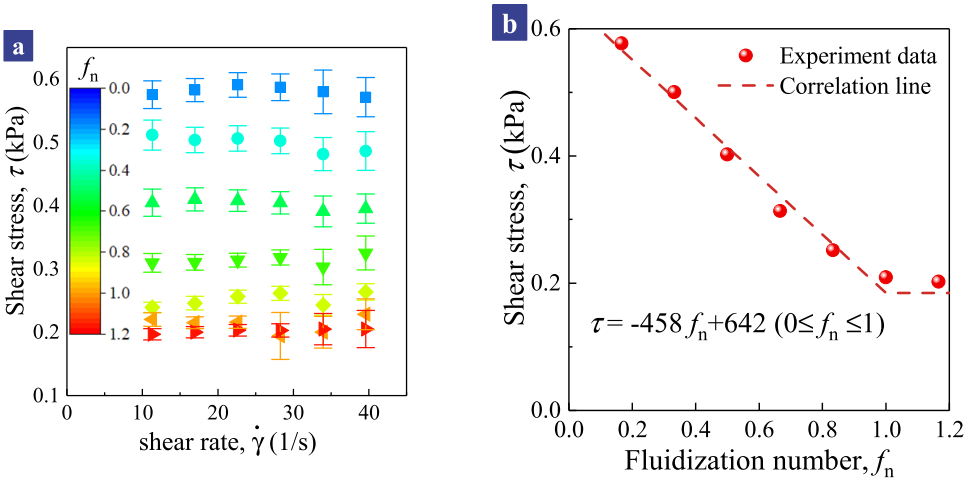

Figure 8. Measurement of particle shear stress. (a) Relationship between the shear stress and the shear rate under different fluidization numbers. (b) Correlation of averaged shear stress and the fluidization number.

https://doi.org/10.1021/acs.iecr.2c04034
Ind. Eng. Chem. Res. 2023, 62, 3001−3010

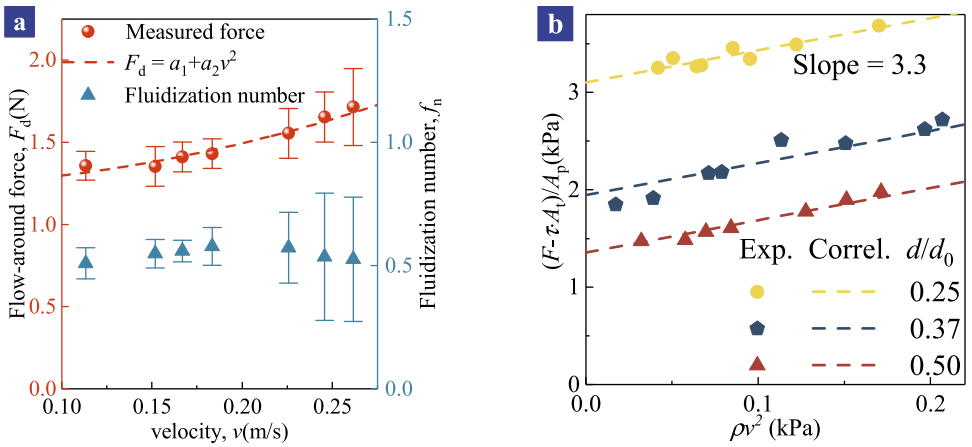

Figure 9. Determination of the relationship between the drag force and the flow velocity. (a) Relationship between the drag force and the flow velocity for a certain obstacle (a cone with the apex angle of 90° and the bottom diameter of 30 mm). (b) Relationship between the drag force and the flow velocity correlated by three groups of data with different size ratios (0.25, 0.37, 0.50, obtained from different obstacles).

minimum fluidization state. In the shear stress measurement system, the gas−solid slip velocity is the apparent gas velocity through the bed, which can be calculated by the ratio of the gas mass flux to the flow area. The minimum fluidization velocity u_{mf} can be determined by an empirical equation,[34] as expressed by eq 8

$$\frac{d_p u_{mf} \rho_g}{\mu_g} = \left[C_1^2 + C_2 \frac{d_p^3 \rho_g (\rho_p - \rho_g) g}{\mu_g^2} \right]^{1/2} - C_1 \tag{8}$$

where C_1 = 33.7, C_2 = 0.0408, d_p is the diameter of flow materials which is adopted as the average diameter d_{50}, ρ_p the particle density, μ_g and ρ_g the viscosity and density of gas phase, and g the gravitational acceleration. The particle shear stress was correlated with the fluidization number and this showed a nearly linear relationship between them when the fluidization number is less than 1 (shown in Figure 8b). Therefore, an empirical correlation was proposed to represent particle shear stress as eq 9

$$\tau = -458 f_n + 642 (0 \le f_n \le 1) \tag{9}$$

where the unit of shear stress τ is Pa. It is worth especially noting that eq 9 was applicable only when $0 \le f_n \le 1$, since when the fluidization number is greater than 1, the particles enter the bubbling fluidization state and it needs another formula to depict.[35] The range of the fluidization number (0−1) also covered that in experimental scenarios (0.38−0.59).

Through this empirical formula (eq 9), the shear stress τ in eq 5 can be calculated. It is worth noting that the calculation method of gas−solid slip velocity u_{slip} in the 3D flow channel mentioned in Section 2.1 is different because of a more complex flow environment. In such a flow channel, the slip velocity needs to be calculated by the pressure drop Δp as indicated by eqs 10 and 11

$$\frac{\Delta p}{L} = 150 \frac{\mu_g (1 - \varepsilon)^3}{\varepsilon^3 d_p^2} u_{slip} + 1.75 \frac{\rho_g (1 - \varepsilon)}{\varepsilon^3 d_p} u_{slip} |u_{slip}| \tag{10}$$

$$\varepsilon = \varepsilon_p + (\varepsilon_{mf} - \varepsilon_p) \frac{|u_{slip}|}{u_{mf}/\varepsilon_{mf}} \tag{11}$$

where eq 10 is the Ergun equation,[36] L is the distance between two pressure measuring points (0.1 m in this experiment system), ε the voidage, and ε_{mf} and ε_p are the voidages in minimum fluidization state and packing state. In eq 11, the voidage in the minimum fluidization state[37] was calculated by an empirical correlation as eq 12

$$\varepsilon_{mf} = \frac{0.586}{\Phi_p^{0.72}} \left(\frac{\rho_g}{\rho_p} \right)^{0.021} \left[\frac{\mu_g^2}{(\rho_p - \rho_g) \rho_g d_p^3 g} \right]^{0.029} \tag{12}$$

where Φ_p is the sphericity viewed as 1 for this flow material. Combined with eqs 7, 8, and 10−12, the fluidization number in a 3D flow channel as demonstrated in Figure 1 can also be calculated.

Through the determination of two stresses (eqs 6 and 9), the drag force from particles can be expressed as eqs 13 and 14

$$F_p = \alpha \rho v^2 A_p \tag{13}$$

$$F_s = (a - b f_n) A_t \tag{14}$$

where A_p and A_t are integral compression and shear areas, respectively, and they can be expressed by eqs 15 and 16

$$A_p = \begin{cases} \frac{1}{4} \pi D^2 & \text{cone} \\ \frac{1}{4} \pi D^2 \sin^2 \theta_2 & \text{sphere} \end{cases} \tag{15}$$

$$A_t = \begin{cases} \frac{1}{4} \pi D^2 \tan \theta & \text{cone} \\ \frac{1}{4} \pi D^2 \tan \theta_1 + \frac{1}{8} \pi D^2 (-\theta_1 + \theta_2 - \sin 2\theta_2) & \text{sphere} \end{cases} \tag{16}$$

where θ is the base angle of the cone and D is the diameter of the bottom surface of the conical obstacle or the diameter of the spherical obstacle. The detailed derivation process of eqs 15 and 16 can be found in the Supporting Material. Combined with eqs 5−16, the components of the drag force from particles, *i.e.*, F_p and F_s, were determined.

Constrained by the experiment condition, the ratio of the characteristic size of the flow-around obstacle to the size of the

https://doi.org/10.1021/acs.iecr.2c04034
Ind. Eng. Chem. Res. 2023, 62, 3001−3010

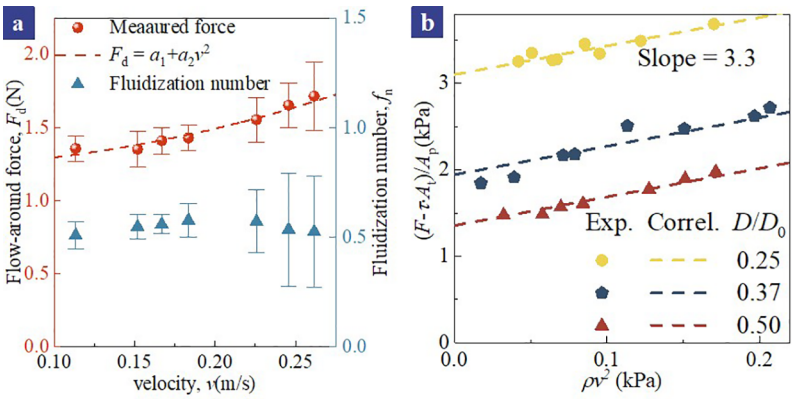

Figure 10. Relation between the pressure fluctuation and the fluctuation of the fluidization number.

flow channel D/D_0 sometimes cannot fulfill the requirement of being less than 0.2, and the confinement force from lateral walls F_c needs to be considered. However, there is no reported model for the calculation of the confinement force. Considering that the size ratio D/D_0 will have a positive influence on the confinement force, it was assumed to be a linear relationship as indicated by eq 17

$$F_c = \frac{D}{D_0} F_{c0} \tag{17}$$

where D is the characteristic length of the obstacle which represents the bottom diameter for the conical obstacle and diameter for the spherical or semispherical obstacle, D_0 is the inner diameter of the flow channel, and F_{c0} is the empirical coefficient. Through the analysis above, the drag force F_d can be calculated by eq 18

$$F_d = F_p + F_s + F_c = \alpha \rho v^2 A_p + (-458 f_n + 642) A_t + \frac{D}{D_0} F_{c0} \tag{18}$$

3.3. Validation of the Proposed Drag Force Model.

The force model proposed in the last section correlates the drag force with the flow velocity as a square relation and with the size ratio D/D_0 as a linear relation, this mathematical form needs proof before the parameter fitting. The relationship between the drag force and the flow velocity was first investigated. Taking a specific obstacle as an example (a cone with the apex angle of 90° and the bottom diameter of 30 mm), the relationship between the drag force and the flow velocity is shown in Figure 9. The square relation (nearly $F_d = a_1 + a_1 v^2$) in Figure 9a preliminarily proves the form of the drag force model. It is worth noting that the uncertainty of the fluidization number increased as the flow velocity increased, since the uncertainty of the pressure drop Δp increased as the flow velocity increased. However, the increasing fluctuation of the pressure drop with the increasing flow velocity is intrinsic for a dense downward particle flow.[38] Thus, the fluctuation of the fluidization number shown in Figure 9a was unavoidable. The fluctuation of the drag force σ_{F_d} was mainly caused by the fluctuation of the fluidization number σ_{f_n}. The relation between these two values of fluctuations in Figure 10 showed a strong dependence which proved this supposition. To give further proof of the formula, fix the size ratio (D/D_0), and address the influence of the velocity on the difference between the drag force and shear force $(F_d - F_s)$, three groups of data with three different size ratios (D/D_0 = 0.25, 0.37, and 0.50, respectively) were applied to make the validation. To intuitively represent the relationship between the drag force and the flow velocity, the force model eq 18 is transformed into eq 19

$$\frac{F_d - F_s}{A_p} = \alpha \cdot (\rho v^2) + \frac{D}{D_0} \frac{F_{c0}}{A_p} \tag{19}$$

where the term $(F_d - F_s)/A_p$ is taken as the dependent variable and the term ρv^2 is taken as the independent variable. The curve shown in Figure 9b indicates a linear relationship between $(F_d - F_s)/A_p$ and ρv^2, proving the square relation between the drag force and flow velocity. The value of the correlated slope (equal to Section 3.3) is thereby assigned to the variable α.

The relationship between the drag force and size ratio was further studied. Since the velocity term in eq 18 is proved, the drag force model can be transformed to better display the influence of the size ratio, as shown by eq 20

$$F_c = F_d - F_p - F_s = F_d - \alpha \rho v^2 A_p - (-458 f_n + 642) A_t \tag{20}$$

where the term $(F_d - F_p - F_s)$ was taken as the dependent variable and the size ratio D/D_0 was taken as the independent variable. All of the experimental data (detailed working conditions will be mentioned in the following text) were applied to correlate eq 20 and the results (shown in Figure 11) indicated a linear relationship, which proves the form of eq 20.

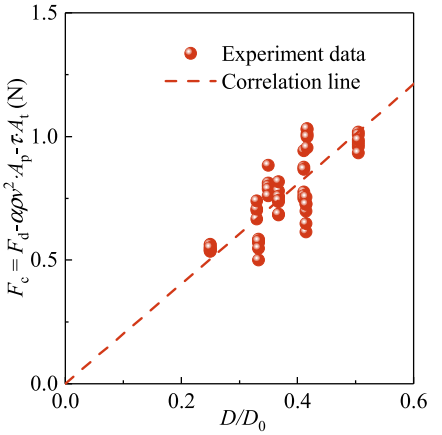

Figure 11. Relationship between the confinement force and the size ratio correlated by experiment data.

https://doi.org/10.1021/acs.iecr.2c04034
Ind. Eng. Chem. Res. 2023, 62, 3001−3010

There exist some deviations in this correlation because the conical obstacles have different heights, but the diameter of the bottom surface was selected as the characteristic length which did not represent the height information. This may partially explain the deviations between the experiments and the model prediction, in particular for the data around D/D_0 = 0.3−0.5. Finding a better characteristic length will be a future study.

With the proof of the mathematical form, data of particles flowing around different obstacles under different velocities were applied to fit the model. Three kinds of obstacles were applied: five conical obstacles with apex angles ranging from 40 to 90° and bottom diameters from 15 to 30 mm, two spherical obstacles with diameters of 20 and 25 mm, and a semispherical sphere (spherical surface upward) with the diameter of 20 mm. The apparent flow velocities range from 0.08 to 0.29 m/s. The fitted parameters of the force model were given by eq 21

$$\begin{cases} \alpha = 3.3 \\ F_{c0} = 2.04\text{N} \end{cases} \tag{21}$$

The experimentally measured drag force on obstacles and the theoretical force calculated by the drag force model (eq 18) with fitted parameters (eq 21) were compared, as shown in Figure 12. The comparison indicates a maximum error of <

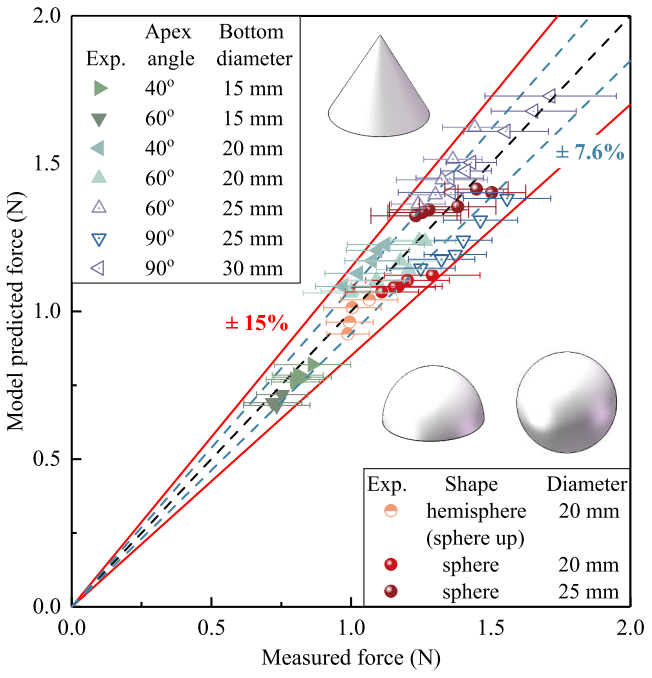

Figure 12. Comparison of experimentally measured force and theoretically calculated force for different working conditions.

±15% and an average error of ±7.6%, which is a rather good agreement for particle flow studies. The errors of measured forces were mainly derived from the fluctuation of the fluidization number which was unavoidable.

4. CONCLUSIONS

In this paper, the flow behaviors of particles downwardly flowing around a certain obstacle were studied and a semiempirical drag force model as per the observed flow characteristics was proposed and validated using the experiment results. The concluding remarks are as follows:

(1) Three featured flow zones, *i.e.*, the flow stagnant zone, the slip-shear flow zone, and the flow separation zone, were identified in the process of dense particles flowing around a triangular obstacle with only the latter two flow zones or a cylindrical obstacle with all flow zones.
(2) The stagnant zone angle and the flow separation angle were independent of flow conditions. The stagnant zone angle was ∼50° and the flow separation angle was ∼130° for the tested glass beads.
(3) The drag force was assumed to consist of the compression force, the shear force from particles, and the confinement force from the lateral wall of the flow channel.
(4) The proposed drag force model was correlated with the experimental data; the maximum calculation error is within ±15% and the average error is ±7.6%.

■ ASSOCIATED CONTENT

Supporting Information

The Supporting Information is available free of charge at https://pubs.acs.org/doi/10.1021/acs.iecr.2c04034.

Detailed derivation process of two integral areas (A_p and A_t, mentioned in Section 3.2) (PDF)
Video of a dense particle flow around a triangular obstacle with the flow velocity of 0.08 m/s (mp4)
Video of a dense particle flow around a cylindrical obstacle with the diameter of 20.12 mm and the flow velocity of 0.15 m/s (mp4)
Video of a dense particle flow around a cylindrical obstacle with the diameter of 20.12 mm and the flow velocity of 0.05 m/s (mp4)
Video of a dense particle flow around a cylindrical obstacle with the diameter of 4.96 mm and the flow velocity of 0.05 m/s (mp4)

■ AUTHOR INFORMATION

Corresponding Author

Yang Zhang − *Key Laboratory for Thermal Science and Power Engineering of Ministry of Education, Department of Energy and Power Engineering, Tsinghua University, Beijing 100084, China;* orcid.org/0000-0003-3297-7433; Phone: +8610 6277 3153; Email: yang-zhang@tsinghua.edu.cn; Fax: +8610 6278 1743

Authors

Xiandong Liu − *Key Laboratory for Thermal Science and Power Engineering of Ministry of Education, Department of Energy and Power Engineering, Tsinghua University, Beijing 100084, China*

Hairui Yang − *Key Laboratory for Thermal Science and Power Engineering of Ministry of Education, Department of Energy and Power Engineering, Tsinghua University, Beijing 100084, China;* orcid.org/0000-0002-0625-7320

Hai Zhang − *Key Laboratory for Thermal Science and Power Engineering of Ministry of Education, Department of Energy and Power Engineering, Tsinghua University, Beijing 100084, China*

Junfu Lyu − *Key Laboratory for Thermal Science and Power Engineering of Ministry of Education, Department of Energy and Power Engineering, Tsinghua University, Beijing 100084, China;* orcid.org/0000-0002-8258-3662

Complete contact information is available at:

https://doi.org/10.1021/acs.iecr.2c04034
Ind. Eng. Chem. Res. 2023, 62, 3001−3010

https://pubs.acs.org/10.1021/acs.iecr.2c04034

Notes

The authors declare no competing financial interest.

■ ACKNOWLEDGMENTS

This study was supported by the National Natural Science Foundation of China (Project no. 52176116) and the National Key R&D Program of China (Project no. 2021YFF0600604). The author Y.Z. received financial support from the Innovation Seed Fund of Shanxi Research Institute for Clean Energy, Tsinghua University.

■ REFERENCES

(1) Yao, Y. G.; Huang, Z.; Zhou, T.; Li, J. J.; Cheng, L.; Zhang, M.; Yang, H. R.; Lyu, J. F. Double-Eccentric Design for the Vortex Finder of a Cyclone Separator. *Ind. Eng. Chem. Res.* **2022**, *61*, 14927−14939.
(2) Barletta, D.; Poletto, M. Pipe stability in aerated silos. *Powder Technol.* **2015**, *277*, 252−261.
(3) Socorro, M.; Machín, A. M.; Verona, J. M.; Santana, D. Hot Gas Filtration and Heat Exchange in a Packed Bed Using Lapilli as a Granular Medium. *Ind. Eng. Chem. Res.* **2006**, *45*, 7957−7966.
(4) Shao, Y.; Agarwal, R. K.; Li, J. G.; Wang, X. D.; Jin, B. S. Computational Fluid Dynamics−Discrete Element Model Simulation of Flow Characteristics and Solids' Residence Time Distribution in a Moving Bed Air Reactor for Chemical Looping Combustion. *Ind. Eng. Chem. Res.* **2020**, *59*, 18180−18192.
(5) Zuriguel, I.; Janda, A.; Garcimartín, A.; Lozano, C.; Arévalo, R.; Maza, D. Silo clogging reduction by the presence of an obstacle. *Phys. Rev. Lett.* **2011**, *107*, No. 278001.
(6) Li, J. G.; Agarwal, R. K.; Yang, B. L. Two-Dimensional Computational Fluid Dynamics Simulation of Heat Removal in Fluidized Bed Methanation Reactors from Coke Oven Gas Using Immersed Horizontal Tubes. *Ind. Eng. Chem. Res.* **2020**, *59*, 981−991.
(7) Xiao, H. L.; Zhang, Y. M.; Hua, Y. Y. A. Oloruntoba, Quantitative comparison of measurement quality of cross-correlation based particle velocity instruments in different gas fluidization regimes. *Adv. Powder Technol.* **2021**, *32*, 3915−3926.
(8) Liu, D. P.; Zhang, S. H.; Wang, R. Y.; Zhang, Y. M. Dynamic forces on a horizontal slat immersed in a fluidized bed of fine particles. *Chem. Eng. Res. Des.* **2017**, *117*, 604−613.
(9) Albert, R.; Pfeifer, M. A.; Barabási, A. L.; Schiffer, P. Slow drag in a granular medium. *Phys. Rev. Lett.* **1999**, *82*, No. 205.
(10) Liu, C. P.; Wan, H. M.; Wang, L. Effect of movement direction on resistance force in granular media. *Powder Technol.* **2019**, *344*, 545−550.
(11) Brzinski III, T. A.; Durian, D. J. Characterization of the drag force in an air-moderated granular bed. *Soft Matter* **2010**, *6*, 3038−3043.
(12) Chehata, D.; Zenit, R.; Wassgren, C. R. Dense granular flow around an immersed cylinder. *Phys. Fluids* **2003**, *15*, No. 1622.
(13) Takada, S.; Hayakawa, H. Drag acting on an intruder in a three-dimensional granular environment. *Granular Matter* **2020**, *22*, No. 6.
(14) Katsuragi, H.; Durian, D. J. Unified force law for granular impact cratering. *Nat. Phys.* **2007**, *3*, 420−423.
(15) Brzinski, T. A.; Mayor, P.; Durian, D. J. Depth-Dependent Resistance of Granular Media to Vertical Penetration. *Phys. Rev. Lett.* **2013**, *111*, No. 168002.
(16) Faug, T. Macroscopic force experienced by extended objects in granular flows over a very broad Froude-number range. *Eur. Phys. J. E* **2015**, *38*, No. 34.
(17) Jiang, Y. J.; Fan, X. Y.; Su, L. J.; Xiao, S. Y.; Sui, J.; Zhang, R. X.; Song, Y.; Shen, Z. W. Experimental validation of a new semi-empirical impact force model of the dry granular flow impact against a rigid barrier. *Landslides* **2021**, *18*, 1387−1402.
(18) Clark, A. H.; Kondic, L.; Behringer, R. P. Particle Scale Dynamics in Granular Impact. *Phys. Rev. Lett.* **2012**, *109*, No. 238302.
(19) Roth, L. K.; Han, E.; Jaeger, H. M. Intrusion into Granular Media Beyond the Quasistatic Regime. *Phys. Rev. Lett.* **2021**, *126*, No. 218001.
(20) Liu, X. D.; Zhang, H.; Yang, H. R.; Zhang, Y.; Lyu, J. F. Validation and evaluation of the CPFD modeling of dense particle flow velocity: Taking particle flow around an obstacle as an example. *Chem. Eng. J.* **2023**, *453*, No. 139719.
(21) Colafigli, A.; Mazzei, L.; Lettieri, P.; Gibilaro, L. Apparent viscosity measurements in a homogeneous gas-fluidized bed. *Chem. Eng. Sci.* **2009**, *64*, 144−152.
(22) Tardos, G. I.; McNamara, S.; Talu, I. Slow and intermediate flow of a frictional bulk powder in the Couette geometry. *Powder Technol.* **2003**, *131*, 23−39.
(23) Yagmur, S.; Dogan, S.; Aksoy, M. H.; Goktepeli, I.; Ozgoren, M. Comparison of flow characteristics around an equilateral triangular cylinder via PIV and Large Eddy Simulation methods. *Flow Meas. Instrum.* **2017**, *55*, 23−36.
(24) Bartsch, P.; Zunft, S. Numerical investigation of dense granular flow around horizontal tubes: Qualification of CFD model with validated DEM model. *Sol. Energy* **2019**, *182*, 298−303.
(25) Niegsch, J.; Köneke, D.; Weinspach, P. M. Heat transfer and flow of bulk solids in a moving bed. *Chem. Eng. Process* **1994**, *33*, 73−89.
(26) Pearce, J. C.; Sabersky, R. H. Thermal wake and separation point for the flow of a granular medium around a heated cylinder. *Lett. Heat Mass Transfer.* **1977**, *4*, 1−8.
(27) Baker, J.; François, G.; Benjy, M.; Itai, E. X-ray rheography uncovers planar granular flows despite non-planar walls. *Nat. Commun.* **2018**, *9*, No. 5119.
(28) Seguin, A.; Bertho, Y.; Gondret, P. Influence of confinement on granular penetration by impact. *Phys. Rev. E* **2008**, *78*, No. 010301.
(29) White, F. M.*Fluid Mechanics*; McGraw-Hill: New York, 2011; pp 482−490.
(30) Takehara, Y.; Fujimoto, S.; Okumura, K. High-velocity drag friction in dense granular media. *Europhy. Lett.* **2010**, *92*, 44003.
(31) Zdravkovich, M. M.*Flow Around Circular Cylinders, Vol 1. Fundamentals*; Oxford University Press, 1997.
(32) Bruni, G.; Barletta, D.; Polettom, M.; Lettieri, P. A rheological model for the flowability of aerated fine powders. *Chem. Eng. Sci.* **2007**, *62*, 397−407.
(33) Yahia, L. A. A.; Piepke, T. M.; Barrett, R.; Ozel, A.; Ocone, R. Development of a virtual Couette rheometer for aeratedgranular material. *AIChE J.* **2020**, *66*, No. e16945.
(34) Wen, C. Y.; Yu, Y. H. A generalized method for predicting the minimum fluidization velocity. *AICHE J.* **1966**, *12*, 610−612.
(35) Chen, S. J.; Cai, R. X.; Zhang, Y.; Yang, H. R.; Zhang, H.; Lyu, J. F. A semi-empirical model to estimate the apparent viscosity of dense, bubbling gas-solid suspension. *Powder Technol.* **2021**, *377*, 289−296.
(36) Ergun, S. Fluid Flow through Packed Columns. *Chem. Eng. Progr.* **1952**, *48*, 89−94.
(37) Geldart, D.; Cullinan, J.; Georghiades, S. The effect of fines on entrainment from gas fluidized beds. *Trans. Inst. Chem. Eng.* **1979**, *57*, 269−275.
(38) Martín, L.; Ommen, J. R. Estimation of the overall mass flux in inclined standpipes by means of pressure fluctuation measurements. *Chem. Eng. J.* **2012**, *204*−*206*, 125−130.